








Research Article

Numerical Analysis of Temperature Deformation Characteristics for Super-High Arch Dams considering Solar Radiation Effects

Chenfei Shao ^{1,2,3,4,5}, Sen Zheng ^{1,2,3}, Chongshi Gu ^{1,2,3}, Shiguang Tian ⁶,
Hao Gu ^{1,2,3}, Yanxin Xu ^{1,2,3,4} and Yuan Wang ^{1,2,3,4}

¹The National Key Laboratory of Water Disaster Prevention, Hohai University, Nanjing 210098, China

²College of Water Conservancy and Hydropower Engineering, Hohai University, Nanjing 210098, China

³National Engineering Research Center of Water Resources Efficient Utilization and Engineering Safety, Hohai University, Nanjing 210098, China

⁴College of Civil and Transportation Engineering, Hohai University, Nanjing 210098, China

⁵Cooperative Innovation Center for Water Safety & Hydro Science, Hohai University, Nanjing 210098, China

⁶Shandong Electric Power Engineering Consulting Institute Corp., Ltd., Jinan, Shandong 250013, China

Correspondence should be addressed to Chenfei Shao; shao_chen_fei@hhu.edu.cn

Received 19 July 2023; Revised 28 September 2023; Accepted 29 September 2023; Published 9 October 2023

Academic Editor: Sara Casciati

Copyright © 2023 Chenfei Shao et al. This is an open access article distributed under the Creative Commons Attribution License, which permits unrestricted use, distribution, and reproduction in any medium, provided the original work is properly cited.

Considering that the effect of solar radiation on the super-high arch dam temperature field remains poorly studied, the calculation accuracy of dam temperature deformation is unable to be guaranteed accordingly. To address the issue, the solar radiation effect is adequately taken into consideration by proposing a practical calculation method based on the ray-tracing algorithm, the precomputation algorithm, and the ASHRAE clear sky model in this paper. With the aid of the ASHRAE clear sky model, the solar radiation received by the super-high arch dam and reservoir water is calculated. The shading effects are calculated by means of the ray-tracing algorithm, and the precomputation technology is introduced to further enhance the computational efficiency. Finally, to guarantee the authenticity of the calculation results, the dam thermodynamic parameters are inverted by employing the hybrid genetic algorithm. Based on the application in a real-life case, we concluded that around one third of the entire dam radial temperature deformation was attributable to solar radiation during continuous sunny days. The analysis results signify a critical role for taking account of the solar radiation in dam deformation calculation. Furthermore, the practicability and utilization prospect of the proposed method was verified.

1. Introduction

With wide utilization of hydroenergy resources, super-high arch dam construction has aroused public attention in China [1–3]. Due to the remarkable economy and security of the arch dam, it has already become the primary type of dam to be adopted in future hydraulic engineering construction. To our knowledge, the dam safety operation is vital in economic profit increase of the project [4, 5]. Therefore, the actual structural behaviour of the super-high arch dam exists as a traditional issue [6–8]. Deformation is

the most intuitive indicator of the dam performance, which is largely affected by temperature load. However, the effect of solar radiation seems to be commonly ignored when studying the dam temperature [9]. In fact, in view of the mutual masking of mountains and seasonal changes in the solar azimuth angle, the temperature distribution of super-high arch dam is likely to be uneven as a result of variation of solar radiation. Hence, in order to accurately and efficiently analyze the dam temperature deformation characteristic, there remains an urgent need for considering solar radiation effects.

In recent years, a growing number of studies have revealed that solar radiation plays a crucial role in dam temperature and operation behaviour. Therefore, scholars have carried out numerical calculation tasks to analyze the solar radiation effects. Léger et al. [10, 11] and Daoud et al. [12] fully took solar radiation into account when simulating the periodic temperature field and stress distribution of dams, but the variation of solar radiation on some exposed surfaces was ignored. Agullo and Aguado [13] proposed a practical numerical model for the dam thermal analysis by considering the solar radiation. However, the calculation accuracy needs to be improved. Sheibany and Ghaemian [14] built a 3D finite element model to analyze the thermal stresses of the Karaj arch dam. The results demonstrated that solar radiation affects the thermal loads by raising the temperature of the arch dam surface. Santillan et al. [15] simulated the thermal field of concrete dams with the comprehensive concern of the solar radiation, the long-wave radiation exchange, the night cooling effects, and the evaporative cooling. Meyer and Mouvet [16] found that solar radiation and up-stream water influence the thermal behavior of the dam by using the finite element method. Mirzabozorg et al. [17] investigated the effects of direct and indirect solar radiation on thermal distribution of the thin high arch dams. Castilho et al. [18] calculated the hydration process and temperature evolution of an arch dam and eventually analyzed the solar radiation effects. Soltani et al. [19] studied the effects of solar radiation on ambient temperature and investigated the probabilistic risk of arch dam failure under thermal loading. Although the above studies have investigated the solar radiation effects from different perspectives, the shading effects of mountains and the dam itself on the solar radiation, and the influence of solar radiation on the reservoir water temperature have been less explored. This may lead to further problems in precise dam temperature field numerical simulation.

To resolve this problem, much theoretical research has been developed. Žvanut et al. [20] analyzed the dam temperature by considering the shading effects, convection, and solar radiation. Jin et al. [21] proposed a model to calculate the ambient temperature field of arch dam. However, the calculation process of the model was complicated due to the ray-tracing method involved. Zhu et al. [22] calculated the dam stress on the basis of the solar radiation shading algorithm and meteorological conditions at the location of high arch dams. They concluded that the uneven absorption of solar radiation in different regions of the arch dam may lead to the adverse stress of high arch dam.

In summary, the solar radiation effects on super-high arch dam deformation characteristics have rarely been studied directly. Therefore, in this paper, according to the geographical location, topographic features, and climatic conditions of the super-high arch dam, a scientific and reasonable numerical method is presented to calculate the influence of solar radiation on dam temperature deformation. With the aid of the ASHRAE (American Society of Heating, Refrigerating, and Air-Conditioning Engineers) clear sky model, ray-tracing method, and precomputation algorithm, the dam temperature and reservoir water

temperature affected by the solar radiation are calculated (Section 2). Accordingly, the precomputation algorithm is introduced to enhance the calculation accuracy and efficiency. Subsequently, the thermodynamic parameter inversion is performed by the hybrid genetic algorithm to improve the accuracy of the numerical analysis (Section 3). To verify the feasibility and validation of the proposed method, a case study based on the Jinping I super-high arch dam project located in Southwest China was carried out (Section 4). Eventually, some valuable conclusions and forward-looking discussions are drawn in Section 5.

2. Numerical Calculation Method for Deformation Temperature of Super-High Arch Dam under the Influence of Solar Radiation

2.1. Numerical Calculation Method for Solar Radiation Received by the Dam Body and Reservoir Water

2.1.1. ASHRAE Clear Sky Model. The ASHRAE clear sky model has been extensively implemented to calculate the solar radiation for decades. The model primarily solves the solar radiation intensity from the following three aspects: direct radiation, sky diffuse radiation, and reflected radiation [23].

When the weather is clear, the intensity of solar radiation on the Earth's surface can be expressed as

$$G_{ND} = \frac{A}{\exp(B/\sin\beta)} C_N, \quad (1)$$

where G_{ND} is the intensity of direct solar radiation perpendicular to the Earth's surface; A is the intensity of solar radiation at zero air mass; B is the extinction coefficient of the atmosphere; β is the solar altitude angle; and C_N is the atmospheric cleanliness.

The total solar radiation intensity incident on a non-perpendicular surface can be given by

$$G_{t1} = \left[\max(\cos\theta, 0) + CF_{ws} + \rho_g F_{wg} (\sin\beta + C) \right] G_{ND}. \quad (2)$$

The formula for calculating the total solar radiation incident on a vertical surface is provided as follows [21]:

$$G_t = \left[\max(\cos\theta, 0) + \frac{G_{dV}}{G_{dH}} C + \rho_g F_{wg} (\sin\beta + C) \right] G_{ND}, \quad (3)$$

where θ is the angle between the sun's rays and the normal to the inclined plane; C is the ratio of the diffuse radiation on a horizontal surface to the direct radiation from vertical incidence; F_{ws} is the angle coefficient between the surface and the sky; ρ_g is the reflectivity of the surroundings; F_{wg} is the angle coefficient between the surface and the ground; G_{dV} is the sky scattering radiation of the vertical surface; G_{dH} is the sky scattering radiation of the horizontal surface.

The computational formulas of F_{ws} and F_{wg} are generally determined by

$$F_{ws} = \frac{1 + \cos \alpha}{2}, \quad (4)$$

$$F_{wg} = \frac{1 - \cos \alpha}{2},$$

where α is the angle of incidence.

The angles of solar altitude β , the angle of incidence α , and the angle between the sun's rays and the normal to the inclined plane θ are depicted in Figure 1, respectively.

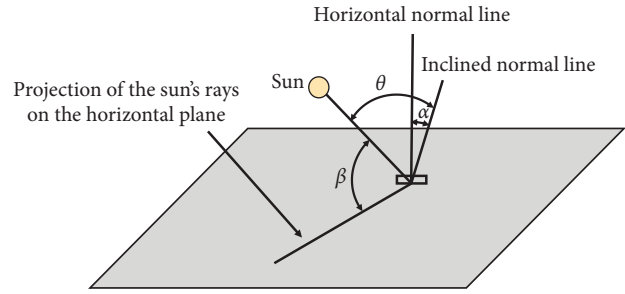


FIGURE 1: Surface solar azimuth and the inclination of any inclined plane.

2.1.2. Numerical Calculation Method for Solar Radiation Received by Super-High Arch Dam Based on Ray-Tracing Algorithm. Owing to the shading effects of towering mountains on solar radiation, the ray-tracing algorithm [24] is introduced to calculate the solar radiation received by the dam body. The ray-tracing algorithm is derived from the principles of geometric optics, and it determines reflection, refraction, and shadow by simulating the propagation path of light rays. First, a ray is generated from the dam surface in the direction of sunlight. Then, it is judged whether the ray intersects with other surfaces. If it intersects, the direct solar radiation is obscured. Otherwise, the solar radiation can be received directly. Considering that the ray-tracing algorithm requires real-time calculation of the shading effects, which involves large unavoidable computational costs. To deal with this problem, the cube acceleration algorithm is introduced. The main steps of solar radiation calculation are introduced as follows [21]:

- (1) Based on the finite element model of the super-high arch dam, the edges of dam surface elements which connect with the air, referred to as free edges, are determined. The free edges are indicated by the red lines in Figure 2.
- (2) In view of the topological information and nodal coordinates of the model, relevant parameters of the free edges can be obtained, such as the normal vector \vec{n} , length, center point coordinates, surface azimuth, and inclination.
- (3) The finite element model can be divided into square grids, and each grid needs to be numbered according to coordinates. A linked list is established on the basis of the free edge numbers contained in each square grid. Figure 3 is the schematic diagram of the established free side linked list (a \rightarrow b \rightarrow c \rightarrow d).
- (4) The solar altitude angle and solar surface azimuth on each specific day during specific time should be calculated.
- (5) Rays can be generated according to the centre point coordinates of each free edge and the result calculated in step (4).
- (6) The square grid numbers that the rays pass through can be calculated subsequently. As illustrated in Figure 4, the grid intersected by the ray emitted from free edge d can be denoted as (2, 5), (3, 5), and (3, 6).

- (7) When the rays intersect with the free edges of the square grids they pass through, it indicates that the solar radiation received by the free edges will be blocked. Otherwise, it will not be blocked.
- (8) By following steps (5)–(7), the shading of solar radiation on all free edges can be determined. On this basis, it is possible to determine the solar radiation received by the dam surface.

2.1.3. Numerical Calculation Method of the Solar Radiation Received by Reservoir Water. Considering the large surface area of the upstream reservoir water is likely to be exposed to prolonged periods of solar radiation, which leads to a substantial variation of the water temperature. Therefore, it becomes vital to investigate the influence of solar radiation on the reservoir water to modify its temperature. The reservoir water and the atmosphere can be perceived as a two-phase coupled thermal system, engaged in continuous heat exchange. The heat flux at the surface of the reservoir can be estimated by (5) [25].

$$\varphi = SR + AR - BR - L - R, \quad (5)$$

where SR stands for the shortwave solar radiation quantity; AR indicates atmospheric longwave radiation quantity; BR represents the longwave radiation quantity emitted by water bodies; L denotes the quantity of heat loss due to evaporation; R is the conductive heat flux. In general, the aforementioned heat exchange process occurs only at the water surface, while the water below the surface only receives solar shortwave radiation.

2.2. Numerical Calculation Method for Dam Temperature Deformation under the Effect of Solar Radiation

2.2.1. Numerical Calculation Method for Reservoir Water Temperature under the Effect of Solar Radiation. For the reservoir water, according to the Bossiness hypothesis, the density changes in the vertical component are considered in the control equation. The density in other formulas is treated as constant, and fluid viscosity is neglected. To better reflect the influence of terrain and the anisotropy of turbulent diffusion, a transformation is applied to the vertical

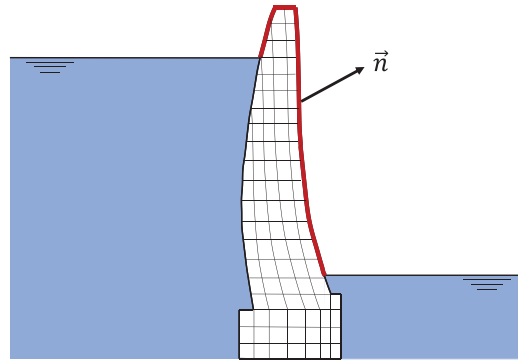


FIGURE 2: The finite model and free edges of the super-high arch dam.

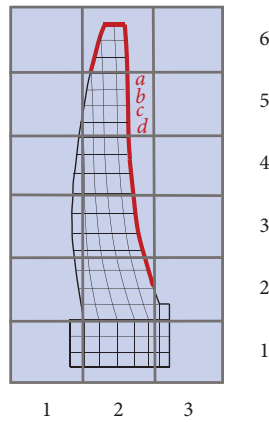


FIGURE 3: Schematic diagram of model space equipartitions.

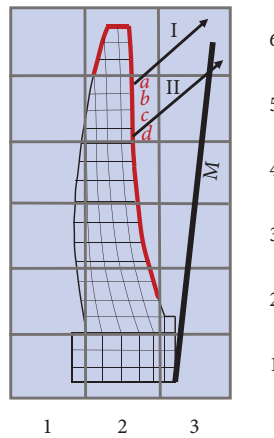


FIGURE 4: The diagram of ray-tracing.

coordinate z . As a result, a new coordinate system σ is introduced, where the Cartesian coordinates are expressed in terms of (x^*, y^*, z^*, t^*) , and the vertical coordinate σ is

expressed in terms of (x, y, σ, t) . The formulas of water temperature control equation can be expressed as follows [26, 27]:

$$\frac{\partial Hu}{\partial x} + \frac{\partial Hv}{\partial y} + \frac{\partial \omega}{\partial \sigma} + \frac{\partial \zeta}{\partial t} = 0, \quad (6)$$

$$\frac{\partial u}{\partial t} + u \frac{\partial u}{\partial x} + v \frac{\partial u}{\partial y} + \omega \frac{\partial u}{\partial \sigma} = fv - \frac{1}{\rho} \frac{\partial p}{\partial x} + \frac{\partial}{\partial x} \left(v_h \frac{\partial u}{\partial x} \right) + \frac{\partial}{\partial y} \left(v_h \frac{\partial u}{\partial y} \right) + \frac{\partial}{\partial \sigma} \left(\frac{v_v}{H^2} \frac{\partial u}{\partial \sigma} \right), \quad (7)$$

$$\frac{\partial v}{\partial t} + u \frac{\partial v}{\partial x} + v \frac{\partial v}{\partial y} + \omega \frac{\partial v}{\partial \sigma} = -fu - \frac{1}{\rho} \frac{\partial p}{\partial y} + \frac{\partial}{\partial x} \left(v_h \frac{\partial v}{\partial x} \right) + \frac{\partial}{\partial y} \left(v_h \frac{\partial v}{\partial y} \right) + \frac{\partial}{\partial \sigma} \left(\frac{v_v}{H^2} \frac{\partial v}{\partial \sigma} \right), \quad (8)$$

$$\frac{\partial \zeta}{\partial t} + \frac{\partial}{\partial x} \left(H \int_0^1 u d\sigma \right) + \frac{\partial}{\partial y} \left(H \int_0^1 v d\sigma \right) = 0, \quad (9)$$

$$\frac{\partial T_w}{\partial t} + u \frac{\partial T_w}{\partial x} + v \frac{\partial T_w}{\partial y} + \omega \frac{\partial T_w}{\partial \sigma} = \frac{\partial}{\partial x} \left(A_H \frac{\partial T_w}{\partial x} \right) + \frac{\partial}{\partial y} \left(A_H \frac{\partial T_w}{\partial y} \right) + \frac{\partial}{\partial \sigma} \left(\frac{A_V}{H^2} \frac{\partial T_w}{\partial \sigma} \right) + Q_T, \quad (10)$$

where x , y , and σ represent the horizontal and vertical coordinates, respectively; u , v , and ω denote the velocity components in the x , y , and σ directions, respectively; t represents time; h is the water depth from the still water level to the bottom; ζ is the displacement of the water surface from the still water level; $H = h + \zeta$ is the total water depth; T_w represents water temperature; $f = 2\Omega \sin\phi$, Ω is the angular velocity of the Earth's rotation, ϕ is the latitude of the location; ρ represents water density; p denotes pressure; v_h and

v_v are the horizontal and vertical eddy viscosity coefficients, respectively; A_H and A_V are the horizontal and vertical thermal diffusivity coefficients, respectively; Q_T represents the source-sink term.

Equations (6)–(9) are the hydrodynamic control equations, and equation (10) is the water temperature convection diffusion equation. If the solar radiation is separated from the heat source term, equation (10) can be written as follows [28]:

$$\frac{\partial T_w}{\partial t} + u \frac{\partial T_w}{\partial x} + v \frac{\partial T_w}{\partial y} + \omega \frac{\partial T_w}{\partial \sigma} = \frac{\partial}{\partial x} \left(A_H \frac{\partial T_w}{\partial x} \right) + \frac{\partial}{\partial y} \left(A_H \frac{\partial T_w}{\partial y} \right) + \frac{\partial}{\partial \sigma} \left(\frac{A_V}{H^2} \frac{\partial T_w}{\partial \sigma} \right) + \frac{1}{\rho c_p H} \frac{\partial SR_z}{\partial \sigma} + Q_T, \quad (11)$$

where c_p represents the specific heat capacity of water, with the unit of J/(kg·°C).

2.2.2. Numerical Calculation Method for Temperature Field of Super-High Arch Dam under the Influence of Solar Radiation. To accurately simulate the dam temperature field, it is of great importance to take the solar radiation effects and shading effects into account. Because the air temperature and reservoir water temperature also vary with the duration of sunlight and seasons, the transient temperature field is introduced to characterize the dam temperature changes.

The finite element format of the dam transient temperature field can be represented as

$$M\dot{\phi} + K_t\phi = P, \quad (12)$$

where M denotes the heat capacity matrix; K_t represents the thermal conductivity matrix; P is the temperature load matrix; ϕ is the array of nodal temperatures; $\dot{\phi}$ is the array of nodal temperature derivatives with respect to time, $\dot{\phi} = d\phi/dt$.

The heat conduction equation is

$$a \left(\frac{\partial^2 T_c}{\partial x^2} + \frac{\partial^2 T_c}{\partial y^2} + \frac{\partial^2 T_c}{\partial z^2} \right) = \frac{\partial T_c}{\partial t}, \quad (13)$$

where a is the temperature diffusivity, $a = \lambda/c\rho_c$; λ denotes the thermal conductivity, c denotes the specific heat; ρ_c is the density of dam concrete; t is time; T_c represents dam temperature; x , y , and z represent the Cartesian coordinates.

When $t=0$, then

$$T(x, y, z, 0) = T_0(x, y, z). \quad (14)$$

The boundary conditions include the following three types:

- (1) The first type of boundary conditions: the boundary temperature.
- (2) The second type of boundary conditions: the heat flux of the boundary.
- (3) The third type of boundary conditions: the convective heat transfer condition on the given boundary.

On the basis of the above analysis, the calculation boundary of the dam temperature field consists of four types (S_1 to S_4), as described in Figure 5.

- (1) Boundary S_1 : dam surface under the water surface.
- (2) Boundary S_2 : dam surface connects with air.
- (3) Boundary S_3 : foundation base surface.
- (4) Boundary S_4 : lateral wall surface of the foundation.

In addition, it is assumed that temperature and heat flux are continuous at the interface. Therefore, the different material parameters determination is fundamental to the calculation.

2.2.3. Numerical Calculation Method for Super-High Arch Dam Deformation under the Influence of Solar Radiation. The comprehensive influence of multiple factors such as solar radiation, shading effects, reservoir water temperature, and air temperature contribute a lot to the temperature deformation of the super-high arch dam. The equilibrium equation for calculating the dam temperature deformation based on the finite element method can be illustrated as follows:

$$K \cdot \delta_T = R_T. \quad (15)$$

The equivalent load vector of the variable temperature nodes is commonly expressed as

$$R_T = \frac{vE}{1-2\mu} \left(\sum_{i=1}^n N_i T_i \right) [1 \ 1 \ 1 \ 0 \ 0 \ 0]^T, \quad (16)$$

where K is the material stiffness matrix; δ_T is the temperature deformation vector; E is the dam elastic modulus; v is the coefficient of linear expansion; μ is Poisson's ratio; N is the shape function of the element; N is the element shape function; T is the element temperature; i denotes the number of the element.

On the basis of the dam temperature field, the temperature deformation at each node can be calculated according to equation (15).

2.3. Inversion Method for the Thermodynamic Parameters of Super-High Arch Dam Based on Hybrid Genetic Algorithm (HGA)

2.3.1. Thermodynamic Parameters Inversion of Super-High Arch Dam. The validity of numerical calculation results depends on the precision of the calculation parameters to a large extent. Based on equations (12) and (13), the calculation parameters of the super-high arch dam include concrete heat capacity c , density ρ_c , thermal conductivity λ , thermal diffusivity a , and heat transfer coefficient τ , etc., [29]

in the dam temperature field calculation. Among them, heat capacity c and density ρ_c can be directly measured by experiments and do not need to be inverted in the numerical simulation. The thermal conductivity λ is affected by the concrete compaction, material properties, and aggregate type, so the above parameters usually need to be determined. Moreover, since $\lambda = ac\rho_c$, only λ and a need to be inverted in general. Because the heat transfer coefficient τ is influenced by factors such as the thermal insulating layer of the dam, τ also needs to be inverted.

The thermodynamic parameters' inversion is to determine the parameters based on the measured response of the dam to the temperature in fact. Therefore, the thermodynamic parameter inversion can be regarded as an optimization process. On the basis of the above analyses, the measured data of thermometers can be fully utilized to invert the dam thermodynamic parameters. By comparing the calculation values and measured values of the temperature at the same locations of the dam and minimizing the errors between the two values, the objective function of the thermodynamic parameter inversion can be established as follows:

$$J(\lambda, \tau) = \sum_{i=1}^M \sum_{j=1}^N (T_{ij}^c - T_{ij}^m)^2, \quad (17)$$

where T_{ij}^c is the calculation value of the dam temperature; T_{ij}^m is the measured value of the dam temperature; M represents the number of monitoring points; N denotes the number of monitoring times.

Consequently, equation (17) converts the parameter inversion problem into a parameter optimization problem. Therefore, HGA as a kind of intelligent optimization algorithm can be employed to invert parameters.

2.3.2. Thermodynamic Parameter Inversion Process Based on HGA. Genetic algorithm (GA) is a computational optimization method inspired by the process of natural selection and evolution. It is based on the principles of genetics and survival of the fittest. However, GA has some limitations, such as slow convergence, premature convergence, and difficulty in handling constraints [30]. To overcome these shortcomings, HGA is presented by combining the principles of GA with niche elimination operation, simplex search algorithm, and accelerating cyclic operation. Accordingly, the quality and efficiency of the parameter inversion can be greatly improved by HGA.

(1) *Niche Elimination Operation.* A niche elimination operation is introduced after the mutation operation. First, the Hamming distance between any two individuals X_i and X_j in the new population can be calculated as follows:

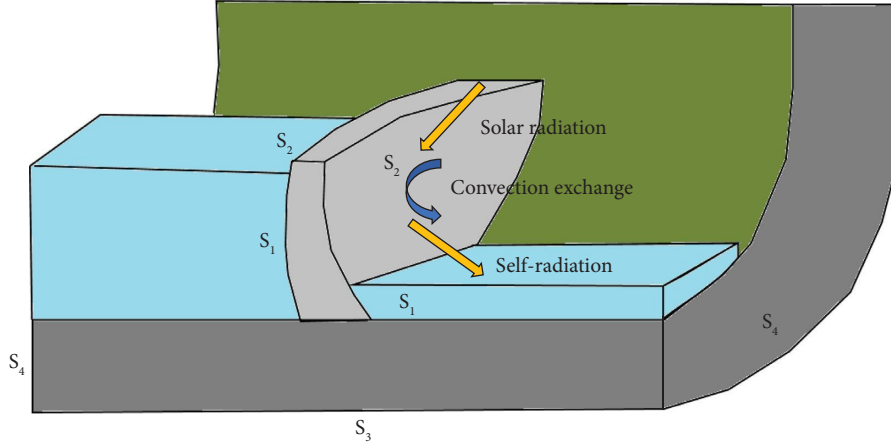


FIGURE 5: Boundary conditions of the arch dam temperature field.

$$\|X_i - X_j\| = \sqrt{\sum_{k=1}^N (x_{ik} - x_{jk})^2}, \quad \{i = 1, 2, \dots, M-1; j = i+1, \dots, M\}, \quad (18)$$

where N is the number of parameters included in each individual.

When the Hamming distance is within a predetermined distance ($\|X_i - X_j\| < L_{lim}$), the fitness of the individuals is compared and the penalty function $F_{\min(X_i, X_j)}$ is applied to individuals with lower fitness to further reduce their fitness.

$$F_{\min(X_i, X_j)} = \text{Penalty}. \quad (19)$$

(2) *Simplex Search Algorithm.* The simplex algorithm starts from an initial simplex in the solution space and can stably search for the optimal solution to the problem through operations such as reflection, expansion, and contraction. After the evolution operation of the genetic algorithm, the first NS best individuals in the offspring population are selected as initial points to form initial simplices and a simplex local search is performed to search for the local optimal solution corresponding to each excellent individual in the current environment. Subsequently, the corresponding individuals in the offspring population are replaced by the optimal solutions to form a new offspring population. Consequently, the overall performance of the population and the local search ability of the algorithm can be enhanced.

(3) *Accelerating Cyclic Operation.* The maximum possible change range of NA excellent individuals generated in the first two evolution operations is utilized to regenerate the initial population of the genetic algorithm and re-evolve. Based on the circulate iteration, the range of the initial population gradually shrinks. Meanwhile, the evolution process is accelerated, the number of iterations is reduced, and the computational cost of the algorithm is reduced.

The thermodynamic parameters inversion process of super-high arch dam based on HGA is as follows:

Step 1: Encoding. The parameters to be inverted (such as thermal conductivity) are genetically encoded, and a counter for the number of evolutionary cycles IT is set to be 1.

Step 2: Population initialization. A set of randomly generated parameter vectors, including $psize$ individuals, is used as the initial population for the algorithm.

Step 3: Objective function calculation. Based on the solution set of the previous generation population, the corresponding objective functions are calculated using the finite element method (FEM). All individuals are ranked according to the size of their objective function values, and the first NP individuals are remembered.

Step 4: Fitness evaluation. The fitness of each individual F_i ($i = 1, 2, \dots, psize$) is calculated based on the above ranking results.

Step 5: Genetic evolution operation. Based on the method described in Section 3.3.2, the parent population is subjected to selection, crossover, mutation, and other operations to produce an offspring population.

Step 6: Niche elimination operation. The Hamming distance between any two individuals X_i and X_j in the new population is calculated based on equation (18). When the Hamming distance is within a predefined distance, the fitness values of the individuals are compared and the penalty function $F_{\min(X_i, X_j)}$ is applied to further reduce the fitness of the individuals with lower fitness values. The individuals are then reranked based on their new fitness values, the new progeny populations are formed by the first $psize$ individuals, and the first NP individuals are remembered.

Step 7: Simplex local search. The first NS individuals in the offspring population obtained by the Niching elimination operation are used as initial points to form an initial simplex for simplex local search. The best solution obtained by the local search is applied to replace the corresponding individual in the offspring population, and a new offspring population is formed.

Step 8: Evolutionary iteration. Return to Step 3 and iterate twice.

Step 9: Accelerated cycle. The above steps constitute the evolutionary iteration process, and the maximum possible range of variation for the first NS individuals in the offspring population obtained after two iterations is used as the initial range for generating the initial population. Return to Step 2 and accelerate the cycle once.

Step 10: Convergence judgment. The convergence is judged based on the criterion that the best objective function value in the population is less than EPS , and the maximum number of allowed evolutionary cycles is used as an auxiliary criterion. If the convergence is not achieved, update the counter $IT = IT + 1$ and return to Step 2. Otherwise, proceed to the following step.

Step 11: Output results. We output the termination iteration number IT and the global optimal value of the parameters to be inverted.

In the above process, the number of individuals in the population $psize$, crossover probability p_c , mutation probability p_m , and other parameters also affect the performance of the algorithm and should be selected based on the specific problem.

3. Case Study

The Jinping I super-high arch dam is located in the Yalong River, spanning the counties of Yanyuan and Muli in Sichuan Province, China. The location of the Jinping I super-high arch dam in Sichuan province is exhibited in Figure 6. It is a key project in the cascade development of hydropower resources in the middle and lower reaches of the Yalong River. The dam is a concrete double-curvature arch dam with a maximum height of 305 meters, making it the highest arch dam in service.

3.1. Finite Element Model of Jinping I Super-High Arch Dam.

Taking Jinping I super-high arch as an example, a finite element model of the dam is established. The model extends 1500 m from the arch beam of the super-high arch dam towards the upstream, downstream, left bank, and right bank and extends 1200 m below the dam foundation. Due to the huge project scale of Jinping I super-high arch dam, the size of the finite element model of the dam foundation should be large enough to reflect the actual scale of the project. Moreover, the calculated dam temperature field is more stable accompanied by the increasing depth of the foundation after many trials. The model adopts eight-node quadratic tetrahedral elements, with 95255 elements and

110648 nodes in all. The dam body is divided into 51083 elements. The horizontal and vertical dimensions of the dam body element mesh are both 9~10 m, and the horizontal and vertical dimensions of the foundation element mesh gradually change from 100 m to 10 m from bottom to top. In fact, the number of elements should be controlled to guarantee the efficiency and effectiveness of numerical simulation. Therefore, the horizontal and vertical dimensions of the foundation element mesh gradually change from 100 m to 10 m from bottom to top to avoid generating too many elements. Furthermore, after many trials, the calculation accuracy cannot be influenced by the large element dimension of the unit away from the dam foundation.

The model accurately depicts the shape of the shape of the actual engineering so that the shading range can be calculated in real time based on the ray-tracing method. The finite element model of the dam is shown in Figures 7(a) and 7(b), and a commercial software named ABAQUS was used to perform the finite element analysis. On account of the smaller area of the downstream water, the effects of the solar radiation on the downstream water temperature could be negligible. Therefore, the focus is mainly on the effects of solar radiation on the upstream water.

3.2. Determination of Thermodynamic Parameters and Environmental Variables.

To calculate the actual solar radiation on the dam surface and reservoir water, the solar altitude angle and azimuth angle at any time should be calculated based on the latitude and longitude of the dam, and then the solar radiation intensity at any time is calculated based on the ASHRAE clear sky model. Combined with the actual situation of the super-high arch dam, the parameters were taken as follows:

- (1) The maximum dam height is 305 m, the dam bottom elevation is 1580 m, the dam crest elevation is 1885 m, the thickness of crown beam top is 16 m, the thickness of crown beam bottom is 63 m, and the thickness of crown beam top is 63 m. The normal water level is 1880 m, the total storage is $7.76 \times 10^9 \text{ m}^3$, the latitude and longitude of the dam site are $28^{\circ}10'49''\text{N}$ and $101^{\circ}37'59''\text{E}$. The upstream surface normal direction of arch crown beam is 25°NE .
- (2) In the ASHRAE clear sky model, the estimated transmittance coefficient C_N can be estimated according to the dam actual location as 0.9, the reflectance coefficient ρ_g is 0.25, and the concrete absorption coefficient ξ is 0.65.
- (3) Table 1 lists the parameter values for the thermodynamic parameters of dam body and foundation.

As the main focus is on the distribution of the dam temperature field, a linear elastic constitutive model is used for both the concrete and the foundation, with material parameters as shown in Table 2. The zoning diagram of the dam body is referred to the construction manual. According to the construction manual, the dam body can be divided into three



FIGURE 6: Schematic diagram of the location of Jinping I super-high arch dam in Sichuan province.

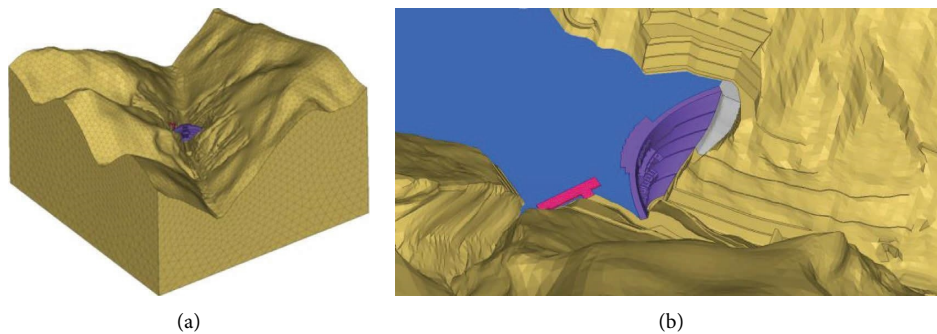


FIGURE 7: The finite element model. (a) Jinping I super-high arch dam. (b) Arch dam and reservoir.

zones which are poured by concrete with varying strength. The corresponding zoning diagram of the dam body is shown in Figure 8.

- (4) Table 3 lists the average monthly air temperature and water temperature for multiple years at the dam site. The annual average number of sunny, cloudy, overcast, rainy, and snowy days at the dam site is illustrated in Table 4. Figure 9 sketches the vertical distribution of water temperature at dam section on typical days in spring, summer, autumn, and winter.

3.3. Boundary Conditions and Precomputation Information.

In the numerical simulation, fixed constraints are applied at the bottom of the model and normal constraints are applied around it. A water temperature convective transfer boundary is applied to the surface covered by the water body, a temperature convective transfer boundary is utilized to the remaining surface, and the solar radiation boundary is adopted to the unshaded area. Finally, the water temperature also needs to be corrected by taking into account the solar radiation effects.

On the basis of the aforementioned calculation steps, it is necessary to compute the shading effects of the dam and water body under typical cases, as well as the corresponding modifications of water temperature under different seasons, water levels, and weather conditions, in order to be directly used in actual calculations. Figures 10 and 11 demonstrate the shading effects of the mountains at different times on the summer solstice and winter solstice, respectively.

From Figures 10 and 11, it can be observed that

- (1) On the summer solstice at 9:00 am, the right bank of the super-high arch dam is shielded, while the left bank continuously receives direct sunlight, resulting in uneven distribution of solar radiation on the dam surface. On the winter solstice at 9:00 am, the dam surface cannot receive direct sunlight due to the shading effects of the mountains and the solar radiation is mainly scattered and reflected in the sky.
- (2) At noon on the summer solstice and the winter solstice, when the solar altitude angle is high, the solar radiation on the dam surface is evenly distributed. However, only a small part of the left bank

TABLE 1: The thermodynamic parameters of dam body and foundation.

Position	Thermal conductivity λ [J·(m·s·°C) ⁻¹]	Specific heat c [J·(kg·°C) ⁻¹]	Surface heat transfer coefficient (air) [W·(m ² ·K) ⁻¹]	Surface heat transfer coefficient (water) [W·(m ² ·K) ⁻¹]
Dam body	1.395	902.3	2	500
Foundation	1.914	766.0	2	500

TABLE 2: The material parameters of dam body and foundation.

Position	Elastic modulus E (GPa)	Poisson ratio μ	Linear expansion coefficient	Density (kg/m ³)
Zone A	30.5	0.167	1×10^{-5}	2400
Zone B	30.2	0.167	1×10^{-5}	2400
Zone C	25.0	0.167	1×10^{-5}	2400
Type II rock of foundation	30	0.2	—	2700
Type III rock of foundation	21	0.25	—	2650

TABLE 3: The average temperature of air and water for multiple years at the dam site.

Month	Temperature of air (°C)	Temperature of water (°C)
January	10.5	5.1
February	13.6	7.2
March	17.4	10.2
April	20.5	13.2
May	21.7	15.7
June	21.9	17.1
July	21.2	17.1
August	21.4	17.2
September	19.2	15.7
October	17.1	13.2
November	12.8	9.1
December	9.1	5.6
Annual mean	17.2	12.2

TABLE 4: The annual mean days of different weathers at the dam site.

Weather	Sunny days	Cloudy days	Rainy and snowy days
The number of days	96	122	147

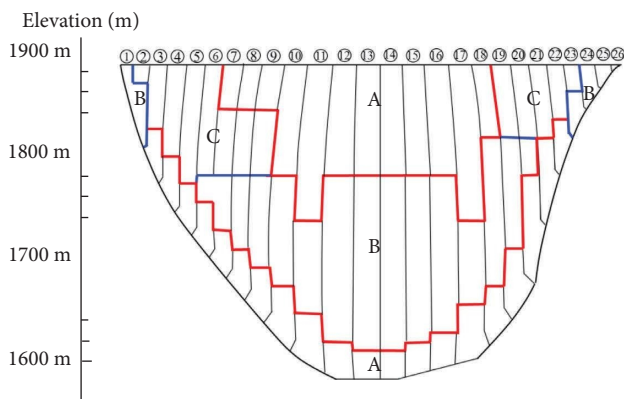


FIGURE 8: The zoning diagram of the dam body.

of the dam can receive direct sunlight due to the shading effects of the mountains, resulting in uneven distribution of solar radiation on the dam surface.

(3) At 3:00 pm on both the summer solstice and the winter solstice, the shading effects of the mountains are not significant, but the super-high arch dam itself has shading effects on solar radiation.

(4) On the summer solstice, the shading effects of the mountains on the water body are small and the upstream water body is exposed to direct sunlight from 9:00 am to 3:00 pm. On the winter solstice, the water body begins to be exposed to direct sunlight in the afternoon and the shading effects of the mountains are more significant.

After obtaining the shading information of the upstream water in typical scenarios, the corresponding water temperature correction information can be obtained through numerical simulation, as depicted in Figure 12.

The impact of solar radiation on the temperature of reservoir water rapidly decreases with increasing depth, and it is generally assumed that it only affects the temperature of the reservoir surface. Because the measured reservoir

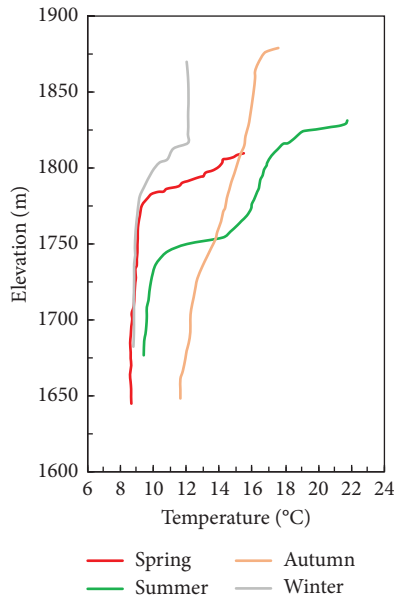


FIGURE 9: Vertical distribution of reservoir water temperature in front of the super-high arch dam on the typical days in different seasons.



FIGURE 10: The solar radiation effects on the summer solstice. (a) At 9:00 am. (b) At 12:00 am.

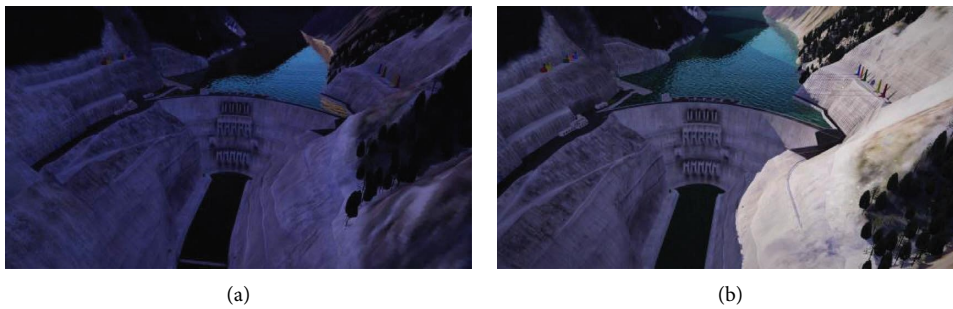


FIGURE 11: The solar radiation effects on the winter solstice. (a) At 9:00 am. (b) At 12:00 am.

temperature is usually a daily average, this seems to be a common problem in accurately reflecting the actual situation of the reservoir temperature under the influence of solar radiation at each moment of the day. For this reason, it is necessary to make corrections to the reservoir temperature at each moment based on the measured reservoir temperature. Particularly, the results of the correction of the pendant reservoir temperature at a certain time based on the

measured pendant reservoir temperature on the summer and winter solstices illustrated are shown in Figure 13.

Because the reservoir water is monitored mainly by the upstream and downstream thermometers embedded in the concrete surface of the dam body, the measured data of reservoir temperature are relatively few. Therefore, the measured results of reservoir temperature are not accurate enough. Moreover, the solar radiation is weaker in winter

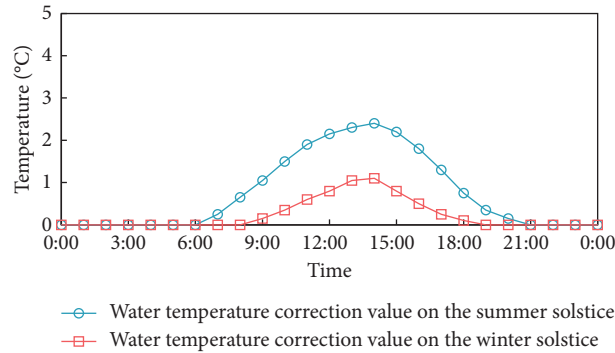


FIGURE 12: The modification curves of reservoir water temperature considering the solar radiation effects.

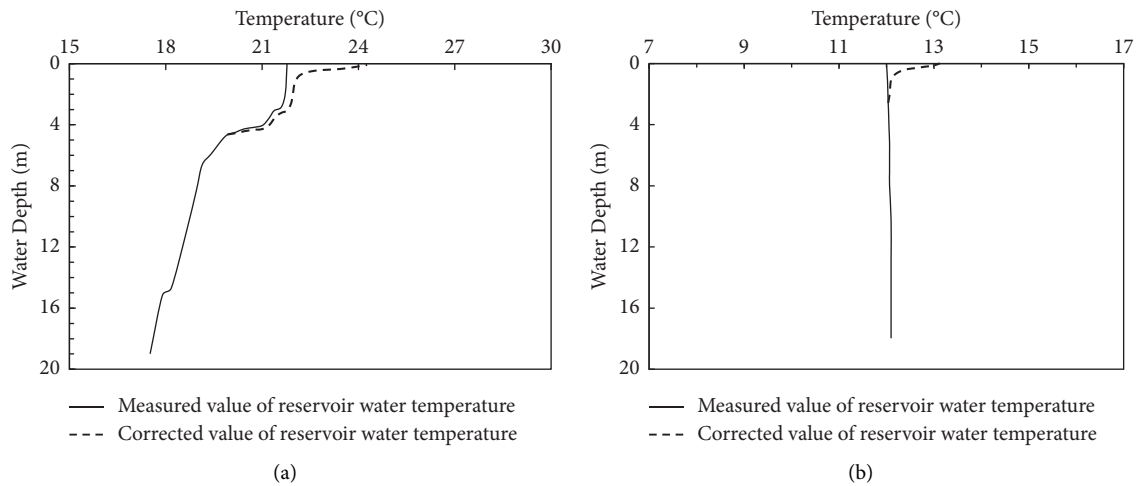


FIGURE 13: Temperature correction values at different time intervals calculated according to the measured values of vertical reservoir water temperature. (a) On the summer solstice. (b) On the winter solstice.

and the temperature of the reservoir is more stable without fluctuation. Therefore, there was no temperature stratification during winter time.

The impact of solar radiation on the temperature field of the dam is relatively small compared to the influence of the ambient temperature. Hence, the basic temperature field under conventional air and water temperature loads was calculated firstly. Then, the boundary conditions $S_1 \sim S_4$ were determined based on measured temperature data. Among them, according to the analysis of the measured data in this area for many years, the basic surface temperature of the foundation S_3 can be taken as 11°C . The base temperature field is the temperature field when the arch dam is sealed. The dam temperature field tends to be stable after five years of pouring, and the influence of solar radiation can be added to this basic temperature field. The base temperature fields in summer and winter are shown in Figures 14 and 15, respectively.

3.4. Numerical Analysis of the Temperature Deformation for the Super-High Arch Dam. On the basis of the shading information of precomputation, it could be determined that

the dam downstream surface is only exposed to small areas on the left bank at noon in winter and the upstream reservoir water is only exposed to the sun for a short time. Calculation results indicate that the effects of solar radiation in winter could be negligible. In summer, the downstream face of the dam on the left bank is exposed to strong solar radiation and the water surface is exposed to the sunlight for a long time.

Figure 16 illustrates the profile of the dam temperature field after being exposed to the sun on the summer solstice. It can be concluded that solar radiation causes the temperature of the dam surface to rise by $2 \sim 3^\circ\text{C}$ and locally up to $4 \sim 5^\circ\text{C}$. Figure 17 depicts the dam temperature field considering the effects of solar radiation on the summer solstice. It can be observed that the downstream face of the dam on the left bank increases in temperature significantly under the influence of solar radiation.

After the sun sets, the dam heat releases, which causes a decrease in the surface temperature of the dam. However, during the hot summer months, the heat absorbed by the dam surface cannot be fully released in the evening and continuous sunny days make the dam surface temperature accumulate. Figure 17 depicts the temperature variation of

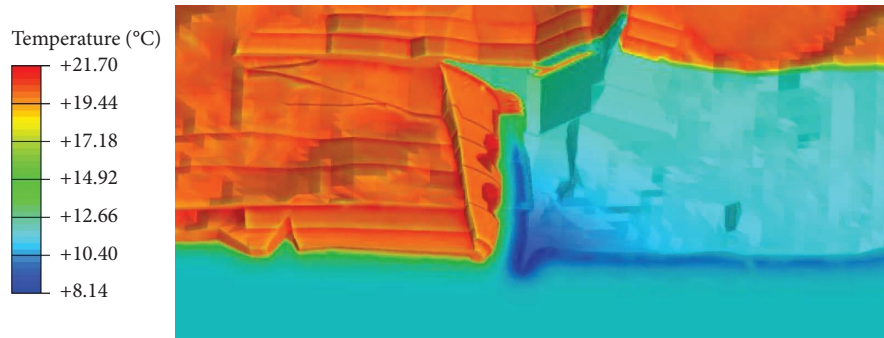


FIGURE 14: Super-high arch dam base temperature field in summer.



FIGURE 15: Super-high arch dam base temperature field in winter.

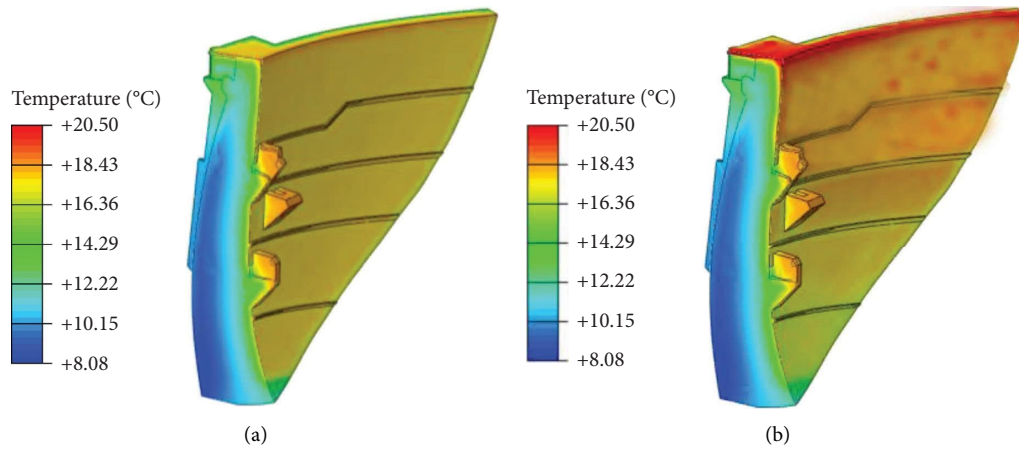


FIGURE 16: Temperature field numerical simulation results of arch crown beam section on the summer solstice. (a) Without consideration of solar radiation. (b) With consideration of solar radiation.

the dam downstream left bank on five continuous sunny days in summer. In Figure 17, the dam surface absolute temperature increases, which results in more heat being released at night, eventually reaching a balance.

In summer, the upper reservoir is greatly influenced by solar radiation and the water surface temperature increases on account of the absorption of heat, which affects the adjacent dam. Figure 18 illustrates the effects of reservoir water temperature correction on the numerical simulation results of dam temperature field in summer. It can be found

that after water temperature correction, the top position of the dam surface temperature increases.

When the sun goes down, as the temperature drops, the dam body begins to exotherm externally, making the dam surface temperature lower. However, during the summer months when the temperature is high, the heat absorbed at the dam surface in the day is not fully released in the evening. When subjected to the solar radiation on continuous sunny days, the dam surface temperature will continue to accumulate. As the absolute dam surface temperature increases,

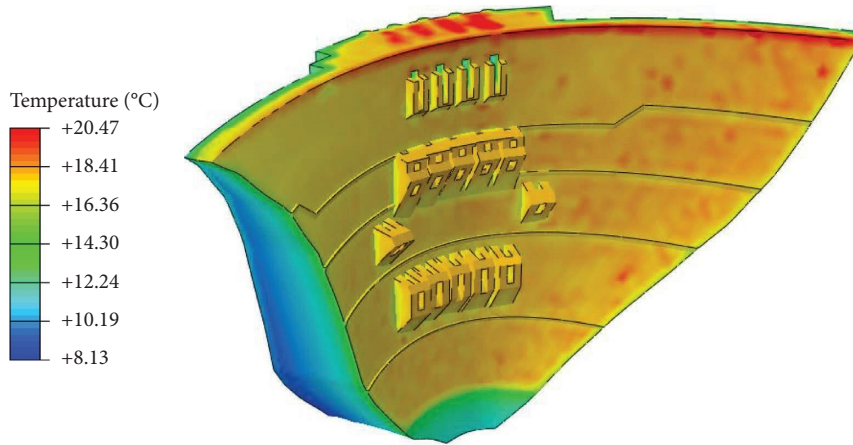


FIGURE 17: The temperature field numerical simulation result of super-high arch dam on the summer solstice.

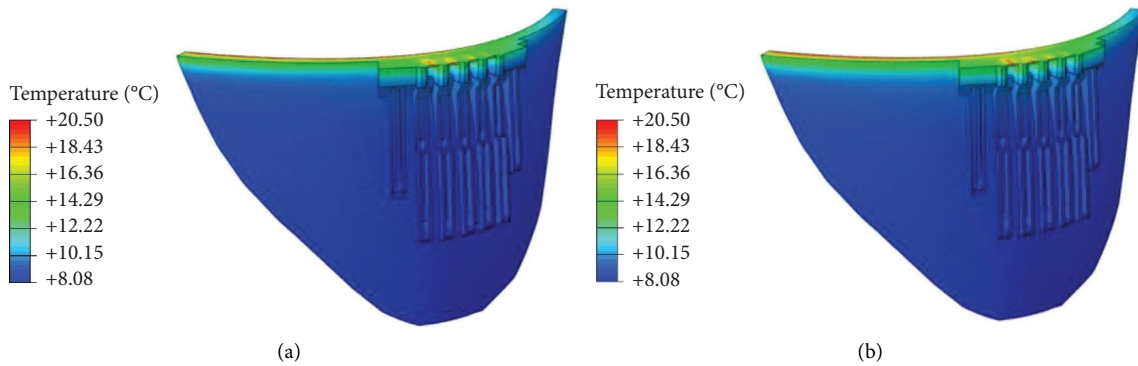


FIGURE 18: Dam temperature field numerical simulation results before and after reservoir water temperature correction on the summer solstice. (a) Before reservoir water temperature correction. (b) After reservoir water temperature correction.

the difference in temperature with the environment increases and the heat released increases in the evening. Nevertheless, an equilibrium is formed to reach the maximum absolute temperature of the dam surface eventually.

Ultimately, the radial deformation field generated when the absolute temperature of the dam reaches its maximum after being affected by solar radiation on multiple consecutive sunny days is exhibited in Figure 19. It can be observed that the maximum upstream deformation of the super-high arch dam influenced by solar radiation was 3.84 mm after continuous sunny days in summer, which is greater compared to the radial deformation generated by the solar radiation on the summer solstice. The dam radial deformation field generated by the influences of air temperature, water temperature, and solar radiation on continuous sunny days is illustrated in Figure 20. The maximum deformation occurred at the crown beam of the arch, with an upstream deformation of 12.61 mm. Therefore, the radial deformation of the dam caused by solar radiation on continuous sunny days accounts for about one-third of the total deformation. It indicates that the influence of solar radiation cannot be ignored when analyzing the super-high arch dam deformation characteristics.

3.5. Thermodynamic Parameter Inversion of Jinping I Super-High Arch Dam

3.5.1. Sensitivity Analysis of Inversion Parameters. Using the finite element model established in Section 3.1, the effects of thermal conductivity of the dam body λ_c , heat transfer coefficient between the dam body and air τ_a^c , heat transfer coefficient between the dam body and reservoir water τ_w^c , heat transfer coefficient between the dam body and foundation τ_f^c , thermal conductivity of the foundation λ_r , thermal conductivity of the mountain λ_s , heat transfer coefficient between the mountain and reservoir water τ_w^s , and heat transfer coefficient between the mountain and air τ_a^s were calculated and the sensitivity of each parameter was determined. Six monitoring points with high, medium, and low elevations on the upstream and downstream faces of dam section 13# were selected, and the ranges of temperature calculation values of all monitoring points were used to analyze the degree of parameter influence. The maximum range was utilized to determine the sensitivity of the parameter, and a larger value indicates a more significant impact on the temperature field. Table 5 lists the ranges of different monitoring points under the influence of various parameters.

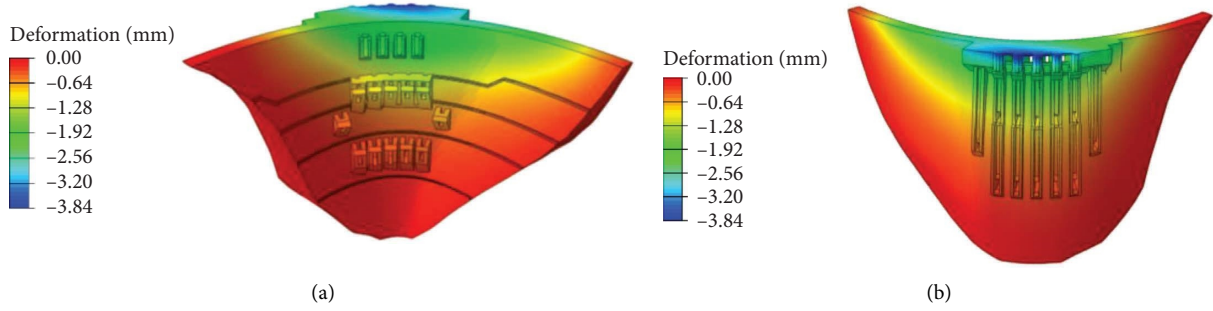


FIGURE 19: Dam radial deformation field considering the solar radiation effects after continuous sunny days in summer. (a) Of the dam upstream surface. (b) Of the dam downstream surface.

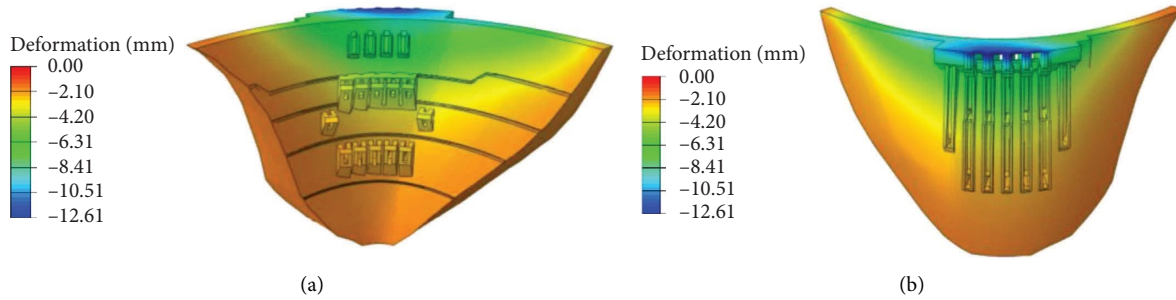


FIGURE 20: Dam radial deformation field considering the continuous influence of air temperature, water temperature, and solar radiation in summer. (a) Of the dam upstream surface. (b) Of the dam downstream surface.

TABLE 5: The range of different indicators under the influence of various parameters.

	R_{T1}	R_{T2}	R_{T3}	R_{T4}	R_{T5}	R_{T6}
λ_c	1.78	1.25	0.52	1.92	1.88	1.59
τ_a^c	2.23	0.13	0.05	2.47	2.35	2.18
τ_w^c	0.24	0.74	0.29	0.08	0.13	0.24
τ_r^c	0.08	0.11	0.21	0.07	0.09	0.13
λ_r	0.03	0.04	0.25	0.02	0.07	0.36
λ_s	0.09	0.05	0.02	0.12	0.09	0.08
τ_w^s	0.06	0.14	0.12	0.03	0.02	0.05
τ_a^s	0.11	0.01	0.01	0.13	0.11	0.12

3.5.2. *Information about the Project.* In the inversion analysis, the measured data of thermometers at dam sections 9# and 13# were applied. There are 138 thermometers (T9-1~T9-138) and 161 thermometers (T13-1~T13-161) installed in the dam section 9# and dam section 13#, respectively. The thermometer layouts of dam section 9# and 13# are illustrated in Figure 21. Figure 22 demonstrates the measured temperature-time curves of the thermometer T13-36, T13-35, and T13-33, which are located near the downstream face, slightly away from the downstream face, and in the middle of the dam body at dam section 13#, respectively. The specific locations of the above three thermometers are marked by yellow stars in Figure 21. As observed in Figure 22, the temperature close to the downstream face varies significantly, while the temperature somewhat distant from the downstream face first increases before stabilizing. In contrast, the temperature in the centre of the dam body is comparatively consistent.

3.5.3. *Calculation Model, Load, and Boundary Conditions.* The finite element model constructed in Section 3.1 is applied for the temperature field inversion analysis, which accurately characterizes the shape of the actual engineering, excavation of the slope, and surrounding mountain shape, and helps improve the accuracy of parameter inversion. The temperature load applied in numerical simulation includes air temperature, reservoir water temperature, and solar radiation. Fixed constraints are applied to the bottom of the model, normal constraints are used to the surrounding areas, water temperature convection and conduction boundary conditions are applied to the surface covered by water, air temperature convection and conduction boundary conditions are utilized to the remaining surfaces, and solar radiation boundary conditions are applied to unobstructed areas. Furthermore, the water temperature needs to be modified by considering solar radiation effects, and the temperature of the dam foundation can be taken as 11°C.

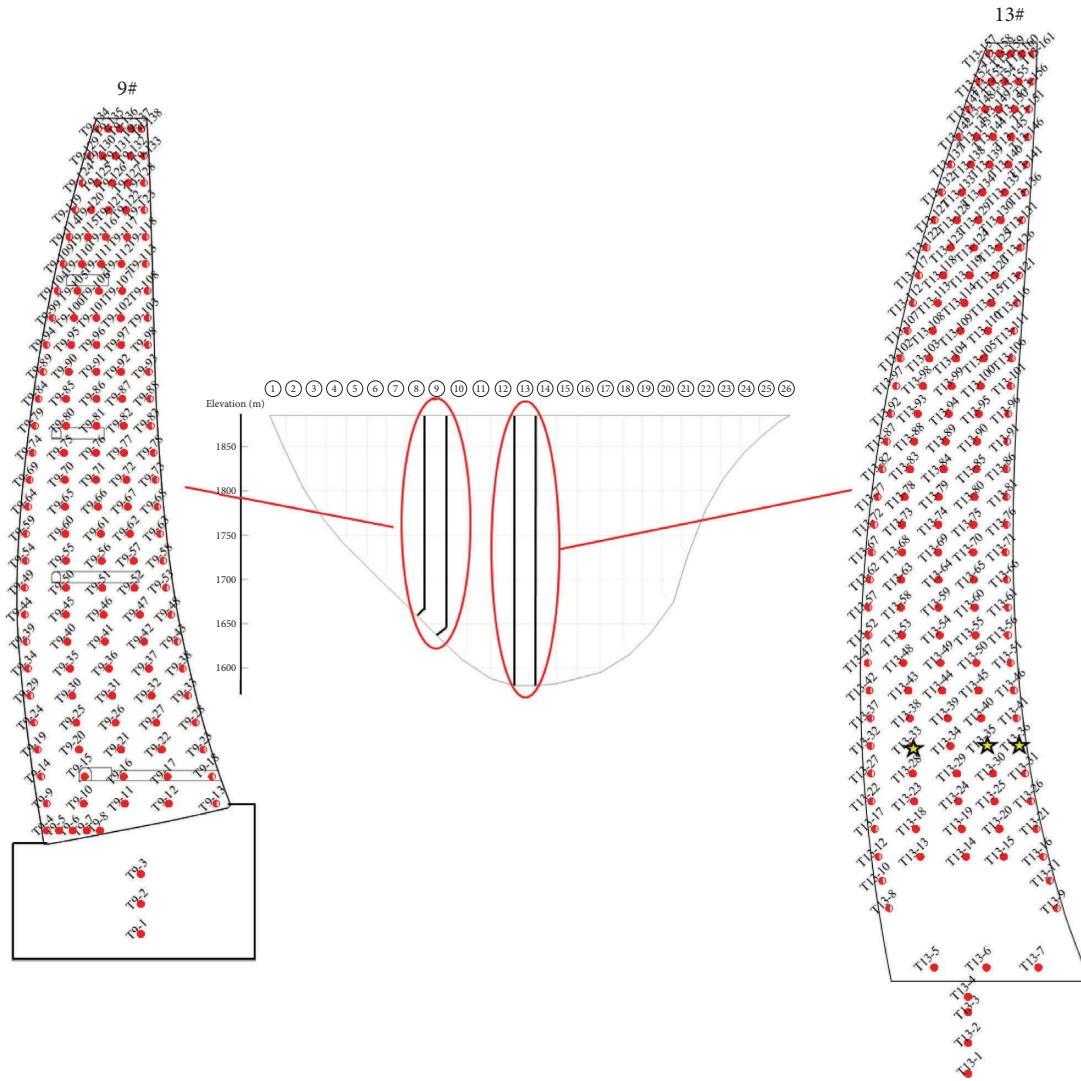


FIGURE 21: The location of thermometers in the dam sections 9# and 13#.

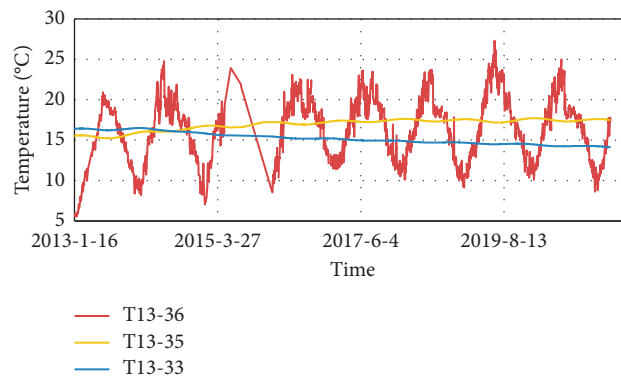


FIGURE 22: The measured temperature process lines of three thermometers at dam section 13#.

3.5.4. *Inversion Analysis Results.* After determining the required data, calculation loads, boundary conditions, etc., for inversion analysis and using the hybrid genetic algorithm introduced in Section 2.3.2 for inversion, the inversion

results are illustrated in Table 6. Figure 23 shows the comparison between the measured and the calculated temperature process lines at a thermometer near the downstream side of dam section 13#. It can be seen that the

TABLE 6: Inversion results of dam temperature field thermodynamic parameters.

Parameter	Unit	Value range		Terminal value
		Lower limit	Upper limit	
Thermal conductivity of dam body λ_c	[J/(m·s·°C)]	0.5	3	1.402
Heat transfer coefficient between dam and air τ_a^c	[W/(m ² ·K)]	1	5	2.342

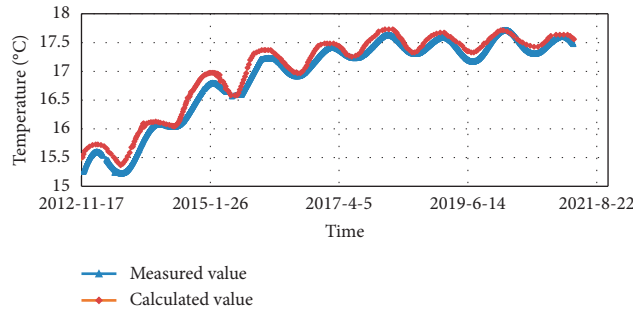


FIGURE 23: The measured and calculated temperature process line of a thermometer in the middle of dam section 13# near the downstream side.

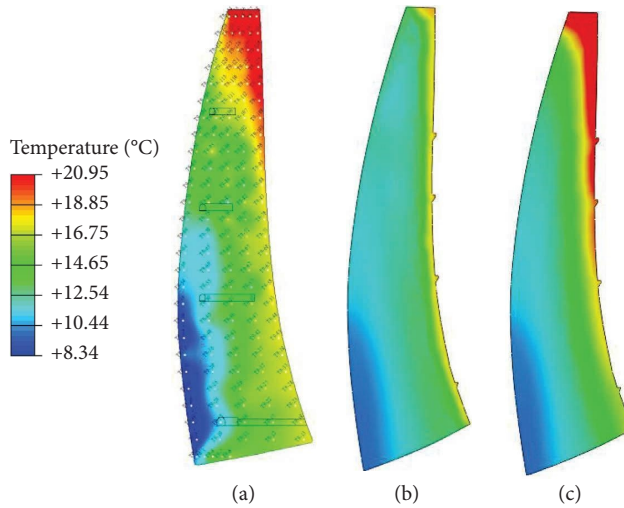


FIGURE 24: The temperature field of 9# dam section. (a) The measured temperature field. (b) The calculated temperature field without consideration of solar radiation effects. (c) The calculated temperature field considering the influence of solar radiation.

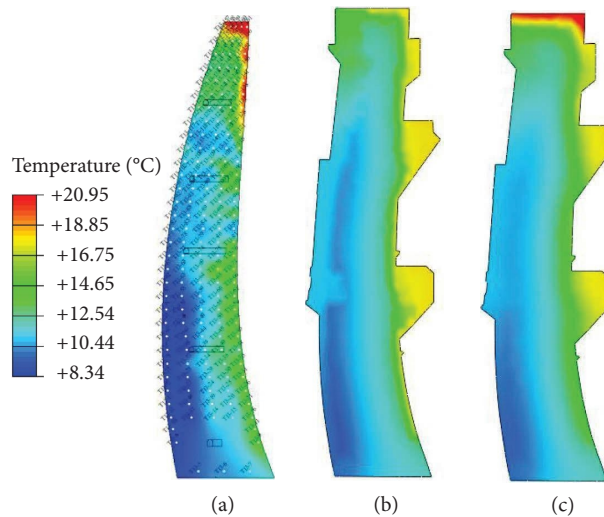


FIGURE 25: The measured and calculated temperature field of 13# dam section. (a) The measured temperature field. (b) The calculated temperature field without consideration of solar radiation effects. (c) The calculated temperature field considering the influence of solar radiation.

calculated value is quite consistent with the measured value, indicating that the inversion results are accurate. Because the joint closure temperature of the super-high arch dam is low and the dam concrete is thick, it takes a long time to reach a quasistable temperature field. Consequently, the temperature increases in the first five years and afterward keeps constant.

Afterwards, the numerical simulations were conducted by incorporating and excluding the effects of solar radiation, and the computed temperature fields were compared with the measured temperature fields as shown in Figures 24 and 25. It can be found that considering solar radiation results in a computed temperature field that is closer to the measured temperature field and better represents the actual temperature distribution of the dam, while the computed temperature field obtained without considering solar radiation cannot accurately depict the actual temperature field of the dam. In addition, the comparison between Figures 24 and 25 represents that the effects of solar radiation are more pronounced of dam section 9# than of dam section 13#, which is due to the fact that the left bank is less affected by the shading effects of the mountain.

4. Conclusions

Focusing on the increasing need for exploring the solar radiation effects on dam temperature deformation, in this study, the ASHRAE clear-sky model, ray-tracing algorithm, and precomputation technique are applied to calculate the temperature deformation of super-high arch dam considering solar effects. Furthermore, HGA is presented by introducing niche elimination operation, simplex search algorithm, and accelerating cyclic operation in GA. HGA is utilized to invert the thermodynamic parameters. Finally, the numerical analysis of Jinping I super-high arch dam temperature deformation was carried out based on geographical location, dam geometry, surrounding topography, and date-specific information, which is taken as an engineering example to verify the efficiency of the proposed method. The conclusions can be drawn as follows:

- (1) The reservoir water temperature and its changes play a vital role in the super-high arch dam temperature field below the water level on the upstream dam surface. It results in the uniform temperature distribution at the same elevation of the dam. On the dam surface above the water level, solar radiation and air temperature exert main effects. Additionally, it demonstrates that the intensity of solar radiation and temperature distribution on the upstream dam surface is uneven due to the shading effects of the dam structure and adjacent mountains.
- (2) The temperature distribution of the downstream dam surface in the case study is mainly influenced by solar radiation and air temperature. Moreover, the shading effects of the mountains and dam structure lead to the higher temperature rising on the left bank, causing overall upstream-oriented temperature deformation. Taken together, the proposed method

provides a feasible way to study the temperature fields and deformation characteristics under solar radiation for super-high arch dams located in different positions and orientations.

- (3) The analysis results of the case study demonstrate that the maximum upstream dam deformation caused by solar radiation is 3.84 mm after continuous sunny days in summer. Therefore, the dam radial deformation caused by solar radiation on continuous sunny days accounts for about one-third of the total deformation. When considering the impact of solar radiation on the deformation characteristics of the selected super-high arch dam in the case study, the results consistently indicate that the radial deformation values calculated with consideration of solar radiation are closer to the measured values in summer. Therefore, it is necessary to take into account the impact of solar radiation while assessing deformation characteristics of super-high arch dams during the summer.

Data Availability

The data on cracks used to support the findings of this study are available from the corresponding author upon request. The other data used to support the findings of this study are included within the article.

Conflicts of Interest

The authors declare that there are no conflicts of interest regarding the publication of this paper.

Acknowledgments

This study was financially supported by the National Natural Science Foundation of China (Grant nos. 52209159 and U2243223); the Fundamental Research Funds for the Central Universities (B220201042 and 2016/423252); China Postdoctoral Science Foundation (2023M730934); Nanjing Overseas Educated Personnel Science and Technology Innovation Project Merit-Based Funding Scheme; Basic Scientific Research Funding of State Key Laboratory (Grant no. 522012272); Water Conservancy Science and Technology Project of Jiangsu (Grant no. 2022024); Jiangsu Young Science and Technological Talents Support Project (Grant no. TJ-2022-076).

References

- [1] C. Shao, C. Gu, M. Yang, Y. Xu, and H. Su, "A novel model of dam displacement based on panel data," *Structural Control and Health Monitoring*, vol. 25, no. 1, Article ID e2037, 2018.
- [2] X. Zhang, J. Xiao, Y. Lin, and D. Zhao, "Valley deformation analysis for a high arch dam in Jinsha river," *Arabian Journal of Geosciences*, vol. 14, pp. 1–24, 2021.
- [3] S. Zheng, C. Shao, C. Gu, and Y. Xu, "An automatic data process line identification method for dam safety monitoring data outlier detection," *Structural Control and Health Monitoring*, vol. 29, no. 7, Article ID e2948, 2022.

- [4] C. Shao, E. Zhao, Y. Xu, S. Zheng, and S. Tian, "Genesis analysis of special deformation characteristics for super-high arch dams in the alpine and gorge regions of Southwest China," *Mathematics*, vol. 11, no. 7, Article ID 1753, 2023.
- [5] Y. Zhu, M. Xie, K. Zhang, and Z. Li, "A dam deformation residual correction method for high arch dams using phase space reconstruction and an optimized long short-term memory network," *Mathematics*, vol. 11, no. 9, Article ID 2010, 2023.
- [6] W. Cao, Z. Wen, and H. Su, "Spatiotemporal clustering analysis and zonal prediction model for deformation behavior of super-high arch dams," *Expert Systems with Applications*, vol. 216, Article ID 119439, 2023.
- [7] J. Hu and F. Ma, "Zoned deformation prediction model for super high arch dams using hierarchical clustering and panel data," *Engineering Computations*, vol. 37, no. 9, pp. 2999–3021, 2020.
- [8] M. Zhu, B. Chen, C. Gu, Y. Wu, and W. Chen, "Optimized multi-output LSSVR displacement monitoring model for super high arch dams based on dimensionality reduction of measured dam temperature field," *Engineering Structures*, vol. 268, Article ID 114686, 2022.
- [9] J. Pan, W. Liu, J. Wang, F. Jin, and F. Chi, "A novel reconstruction method of temperature field for thermo-mechanical stress analysis of arch dams," *Measurement*, vol. 188, Article ID 110585, 2022.
- [10] P. Léger, J. Venturelli, and S. S. Bhattacharjee, "Seasonal temperature and stress distributions in concrete gravity dams. Part 1: modelling," *Canadian Journal of Civil Engineering*, vol. 20, no. 6, pp. 999–1017, 1993.
- [11] P. Léger, J. Venturelli, and S. S. Bhattacharjee, "Seasonal temperature and stress distributions in concrete gravity dams. Part 2: behaviour," *Canadian Journal of Civil Engineering*, vol. 20, no. 6, pp. 1018–1029, 1993.
- [12] M. Daoud, N. Galanis, and G. Ballivy, "Calculation of the periodic temperature field in a concrete dam," *Canadian Journal of Civil Engineering*, vol. 24, no. 5, pp. 772–784, 1997.
- [13] L. Agullo and A. Aguado, "Thermal behavior of concrete dams due to environmental actions," *Dam Engineering*, vol. 6, pp. 3–21, 1995.
- [14] F. Sheibany and M. Ghaemian, "Effects of environmental action on thermal stress analysis of Karaj concrete arch dam," *Journal of Engineering Mechanics*, vol. 132, no. 5, pp. 532–544, 2006.
- [15] D. Santillán, E. Saleté, D. J. Vicente, and M. Á. Toledo, "Treatment of solar radiation by spatial and temporal discretization for modeling the thermal response of arch dams," *Journal of Engineering Mechanics*, vol. 140, no. 11, Article ID 5014001, 2014.
- [16] T. Meyer and L. Mouvet, "Behaviour analysis of the Vieux-Emosson arch gravity dam under thermal loads," *Dams Engineering*, vol. 6, pp. 275–292, 1995.
- [17] H. Mirzabozorg, M. A. Hariri-Ardebili, M. Shir Khan, and S. M. Seyed-Kolbadi, "Mathematical modeling and numerical analysis of thermal distribution in arch dams considering solar radiation effect," *The Scientific World Journal*, vol. 2014, Article ID 597393, 15 pages, 2014.
- [18] E. Castilho, N. Schlar, C. Tiago, and M. L. B. Farinha, "FEA model for the simulation of the hydration process and temperature evolution during the concreting of an arch dam," *Engineering Structures*, vol. 174, pp. 165–177, 2018.
- [19] N. Soltani, M. Alembagheri, and M. H. Khaneghahi, "Risk-based probabilistic thermal-stress analysis of concrete arch dams," *Frontiers of Structural and Civil Engineering*, vol. 13, no. 5, pp. 1007–1019, 2019.
- [20] P. Žvanut, G. Turk, and A. Kryżanowski, "Effects of changing surrounding conditions on the thermal analysis of the Moste concrete dam," *Journal of Performance of Constructed Facilities*, vol. 30, no. 3, Article ID 4015029, 2016.
- [21] F. Jin, Z. Chen, J. Wang, and J. Yang, "Practical procedure for predicting non-uniform temperature on the exposed face of arch dams," *Applied Thermal Engineering*, vol. 30, no. 14–15, pp. 2146–2156, 2010.
- [22] Z. Zhu, Y. Liu, and Y. Tan, "Simulation of temperature field of high arch dams considering solar radiation[C] IOP Conference Series: Earth and Environmental Science," *IOP Conference Series: Earth and Environmental Science*, vol. 455, no. 1, Article ID 12003, 2020.
- [23] S. A. Al-Sanea, M. F. Zedan, and S. A. Al-Ajlan, "Adjustment factors for the ASHRAE clear-sky model based on solar-radiation measurements in Riyadh," *Applied Energy*, vol. 79, no. 2, pp. 215–237, 2004.
- [24] E. M. Vitucci, F. Falaschi, and V. Degli-Esposti, "Ray tracing algorithm for accurate solar irradiance prediction in urban areas," *Applied Optics*, vol. 53, no. 24, pp. 5465–5476, 2014.
- [25] H. T. Ren, *Numerical Simulation of Water Temperature in Large Reservoirs*, Ocean Press, Beijing, China, 2010.
- [26] X. M. Guo, L. Kang, and T. B. Jiang, "A new depth-integrated non-hydrostatic model for free surface flows," *Science China Technological Sciences*, vol. 56, no. 4, pp. 824–830, 2013.
- [27] A. K. M. Q. Ahsan and A. F. Blumberg, "Three-dimensional hydrothermal model of onondaga lake, New York," *Journal of Hydraulic Engineering*, vol. 125, no. 9, pp. 912–923, 1999.
- [28] T. A. El-Mihoub, A. A. Hopgood, L. Nolle, and A. Battersby, "Hybrid genetic algorithms: a review," *Engineering Letters*, vol. 13, no. 2, pp. 124–137, 2006.
- [29] Z. F. Yu, X. Y. Zhang, L. J. Liu, and Y. R. Chen, "Inverse analysis of mass concrete thermal parameter based on genetic algorithm," *Journal of Architecture and Civil Engineering*, vol. 32, no. 5, pp. 81–88, 2015.
- [30] E. K. Aydogan, I. Karaoglan, and P. M. Pardalos, "HGA: hybrid genetic algorithm in fuzzy rule-based classification systems for high-dimensional problems," *Applied Soft Computing*, vol. 12, no. 2, pp. 800–806, 2012.